Publications of the Astronomical Society of the Pacific, 128:055001 (12pp), 2016 May doi:10.1088/1538-3873/128/963/055001

Qualification and Testing of a Large Hot Slumped Secondary Mirror for Schwarzschild–Couder Imaging Air Cherenkov Telescopes

G. Rodeghiero[1,2], E. Giro[1], R. Canestrari[3], C. Pernechele[1], G. Sironi[3], G. Pareschi[3], L. Lessio[1], and P. Conconi[3]
[1] INAF OAPD, Vicolo Osservatorio 5, I-35122 Padova, PD, Italy
[2] Max-Planck-Institut für Astronomie, Königstuhl 17, D-69117 Heidelberg, Germany; rodeghiero@mpia.de
[3] INAF OAB, Via E. Bianchi 46, I-23807 Merate, LC, Italy
Received 2015 November 21; accepted 2016 January 4; published 2016 March 25

Abstract

Dual-mirror Schwarzschild–Couder (SC) telescopes are based on highly aspherical optics, and they represent a novel design in the world of very high energy astrophysics. This work addresses the realization and the qualification of the secondary mirror for an SC telescope, named ASTRI, developed in the context of the Cherenkov Telescope Array Observatory. The discussion surveys the overall development from the early design concept to the final acceptance optical tests.

Key words: gamma rays: general – techniques: image processing – telescopes

Online material: color figures

1. Introduction

Very high energy (VHE; ≥ 100 GeV) astrophysics and astroparticle physics are young and continuously developing fields that probe the non-thermal and extreme Universe. Thanks to the advent of cornerstone space missions as the *Fermi* (Atwood et al. 2009) and *AGILE* (Tavani et al. 2008) satellites and to the construction of ground-based detectors as Imaging Air Cherenkov Telescopes (IACTs) and Extensive Air Shower (EAS) detectors (De Angelis et al. 2008), the gamma-ray astronomy has unlocked a new, unprobed window into the high-energy (HE; ≥ 100 MeV) universe. All the detectors observing the gamma-ray sky operate in a photon-limited regime, and the statistics of gamma-ray photons is so poor that it is impossible to concentrate the photons; this leads to telescopes radically different from those observing at larger wavelengths (De Angelis et al. 2008). Satellites typically have very limited effective area and low sensitivity, but they have large duty cycle and low background noise. Conversely, ground-based detectors, which exploit the Earth's atmosphere as part of the detection system, have a large effective area and consequently a high sensitivity, but suffer low duty cycles and high background. Satellites observe in the MeV–GeV range, while ground-based detectors can detect photons with energies between GeV and TeV, and best results can be achieved operating the two techniques in synergy to provide a wide energy coverage.

Between the ground-based detector families, the most sensitive technique is based on the IACTs. These telescopes detect the Cherenkov radiation emitted by superluminal particles inside air showers, initiated by a primary γ-ray photon colliding with the atoms of the upper troposphere. The originated Cherenkov light cone that propagates into the atmosphere creates a light pool at the ground of about 120 m in radius, and the higher the energy of the primary γ-ray the larger the number of photons released; the reader can refer to Jelley & Porter (1963) for detailed insight in the Cherenkov phenomenology. The atmospheric air shower has a duration of 2–3 ns at the ground level and the IACTs reflectors are used to collect and concentrate the Cherenkov photons onto the focal plane of an extremely fast camera capable of GHz sampling.

All the IACTs operating today rely on single-mirror solutions, which are mostly based on parabolic designs, like the MAGIC (Doro et al. 2008) telescopes or Davies–Cotton configuration like VERITAS (Weekes et al. 2002) and H.E.S.S. I (Bernlöhr et al. 2003). Both configurations are implemented on extremely fast optical systems ($\sim F/1$) able to catch elusive Cherenkov light signals. In the last decade, the concept for a new long-term project, the Cherenkov Telescope Array (CTA), has been developed, and it is now entering the construction phase. The CTA Observatory is the new generation facility for ground-based very high energy astrophysics that will provide unprecedented sensitivity over a wide range of gamma-ray energies spanning from 20 GeV to 300 TeV. CTA will provide full-sky coverage by deploying two different arrays: CTA south, the largest infrastructure, for the observation of galactic objects and the galactic black hole and CTA North mainly devoted to the extragalactic sources (Acharya et al. 2013). To achieve this ambitious goal, CTA south[4] will be composed of

[4] CTA North will have the same number of LSTs, but a reduced number of MSTs and no SSTs.

4 large-sized telescopes (LSTs) 24 m in diameter, 25 medium-sized telescopes (MSTs) 12 m in diameter and 50–70 small-sized telescopes (SSTs) 4 m in diameter.

In this context, the Italian National Institute for Astrophysics (INAF) supported by the Italian Ministry of Education, University and Research is carrying out a project, named ASTRI, Astrofisica con Specchi a Tecnologia Replicante Italiana, with the goal of developing an SST prototype proposed to be part of CTA, and based on a Schwarzschild–Couder (SC) optical design. In the CTA scenario, there is a novel interest for the development of dual-mirror configurations following the SC optical design (Vassiliev et al. 2007; Pareschi et al. 2013). This peculiar design, based on two highly aspherical mirrors leads to wide-field, aplanatic telescopes characterized by small $F/\#$ and compact structures. Dual-mirror solutions allow the use of smaller camera pixels (∼3–6 mm) based on silicon photo multipliers (SiPMs) technology in substitution of the larger photo multiplier tubes (PMTs; ∼1 inch) currently in use on IACTs. The increased complexity in terms of manufacturing and alignment of the telescope optics is motivated by the new attractive capabilities of this system such as the reduction of both telescope and camera size and the possibility to use SiPMs as detectors. The SC configuration leads to a large FoV with fewer off-axis aberrations and improved angular resolution over the whole FoV with respect to the single-mirror solutions.

The present work deals with the challenging development, realization, and testing of the secondary mirror of the first dual-mirror, SST prototype, named ASTRI SST-2 M, manufactured with the hot slumping technique.

The discussion begins with a general overview of the IACT designs with focus on the ASTRI SST-2 M prototype (Section 2), then in Section 3, the hot slumping technique is presented in relation to the manufacturing of the large aspherical secondary mirror. In Section 4, the test campaign on the secondary mirror of the ASTRI SST-2 M prototype is extensively discussed, putting in evidence the main results in terms of mirror quality and impact of the surface deviations on the telescope performances.

2. SC Telescopes

The ASTRI Project aims to develop a compact wide-field SST prototype proposed for the CTA Observatory based on an SC configuration. The SC design allows a significant reduction of the plate scale with respect to single-mirror solutions, making it compatible with finely pixelated cameras. All the large IACTs operating today work with the PMTs and the Winston cones that have dimensions in the order of ∼1 inch. The only exception is the FACT telescope that is the first prototype that explores the possibilities of utilizing SiPMs (Biland et al. 2014). ASTRI adopts this new detection technology based on 3 × 3 mm pixels.

The general baseline for the development of IACTs is driven by the need for fast optical systems ($F/\#$ ∼1), large collecting power, wide-field observations, and limited aberrations for the off-axis fields. The need of wide-field imagers is extremely important for SSTs that must guarantee a corrected FoV of∼8°–9° for two reasons: (i) a wide FoV leads to imaging the whole Cherenkov shower and allows the Hillas parameterization of the showers topology (Hillas 1985); (ii) a wide FoV enables monitoring of the gamma-ray activity in large portions of the sky in a single observation and performing an all-sky survey in a relatively short time (Mirzoyan & Andersen 2009). The discrimination between gamma and hadron showers requires angular resolution on the order of $\sim 0\overset{\circ}{.}05$ on the GeV scale and $\sim 0\overset{\circ}{.}1 - 0\overset{\circ}{.}2$ for Cherenkov air showers triggered by TeV γ-rays (Mirzoyan & Andersen 2009). This requirement becomes less stringent and allows larger PSFs for γ-rays at 10–100 TeV where the sensitivity of the ASTRI SST-2 M achieves its maximum.

It is worthwhile to survey the performances (PSF size versus FoV) of prime-focus versus dual-mirror configurations to underline the advantages gained with the latter. The study envisages the most common optical configurations used or proposed for IACTs as spherical, parabolic, DC, Schmidt, and SC telescopes. A schematic of the telescopes' optical design and their PSFs is shown in Figure 16, while the main geometric characteristics are reported in Table 1. Parabolic single-mirror telescopes are configurations widely used in astronomy and IACTs. The DC configuration, inherited from the early solar concentrators (Davies & Cotton 1957), foresees an array of spherical facet mirrors that are all identical and mounted on a spherical structure with a radius of curvature (RoC) R equal to the focal length of the telescope (f). Each facet has the same RoC, $2R$, facilitating fabrication, and alignment, and it is oriented toward a point at $(x, y, z) = (0, 0, 2f)$. The Schmidt telescope has a primary spherical mirror coupled with a refracting, aspherical corrector plate positioned in the RoC of the reflector. The resulting focal plane is curved with the RoC halved with respect to that of the primary mirror and located between the corrector plate and the reflector. The SC configuration is based on two aspherical, concave mirrors (Wilson 1994) providing wide FoV and fast $F/\#$; the focal plane is convex and curved, and located between the primary and secondary mirrors.

The evolution of the PSFs size over the FoV at the focal plane of the different telescopes is shown in Figure 1. Although the telescope PSF size depends on the $F/\#$, this comparative study assumes all the designs having the same–comparable collecting area and angular resolution (4 m class telescopes).

SC and Schmidt configurations lead to more compact solutions with respect to single-mirror telescopes, e.g., the ASTRI SST-2 M prototype has an average angular resolution of $\Delta\theta \sim 0\overset{\circ}{.}16$ and a separation between M1 and M2 of ∼3.2 m. To get the same angular resolution with single-mirror

Table 1
Main Optical Parameters of the Telescopes Considered in the Comparative Study

Surface	Diameter (mm)	Curvature Radius (mm)	Total Track (mm)	$F/\#$
Prime-focus	Spherical			
M1	4300	−20800	10360	2.42
Camera	1780	0		
Prime-focus	Parabolic			
M1	4300	−20800	10400	2.42
Camera	1780	0		
DC				
M1	5000	−20000	10000	2
Camera	1600	0		
Schmidt				
M1	4200	−4300	4310	0.53
Corrector	3772	−6.07e-12[a]		
Camera	360	−2150		
SC				
M1	4306	−8223.8	3215	0.51
M2	1800	2180		
Camera	360	1060		

Notes. Single-mirror solutions equipped with PMTs, having equal collecting area and angular resolution, need larger focal planes with respect to dual-element designs working with SiPMs. Larger cameras and bigger supporting structures require heavier and stiffer mechanical structures that make the cost of the telescope increasing.
[a] Fourth term of the even asphere describing the corrector plate.

telescopes equipped with PMTs (size of ∼1 inch), the required focal length is $f\sim$ 10.4 m. Dual-element solutions guarantee a constant size of the PSF all over the FoV, while the off-axis performances of the single-mirror configurations as spherical and parabolic quickly deteriorate under the effect of aberrations (see Figure 1). The DC, differently from the other single-mirror designs, has the advantage of not deteriorating its performances off-axis even if the linear size of the PSF at the focal plane is on the order of an inch.

Moreover, the single-mirror solutions need larger and heavier cameras to cover the entire FoV with respect to the contained sizes of SC and Schmidt telescopes. The best performing system in terms of corrected FoV and compact PSFs is the Schmidt telescope that has already been proposed by Mirzoyan & Andersen (2009) as an IACT candidate. However as pointed out by Mirzoyan & Andersen (2009) and confirmed by the current comparative study, such a telescope requires a large aspherical corrective plate that would be necessarily segmented and subjected to a complex active

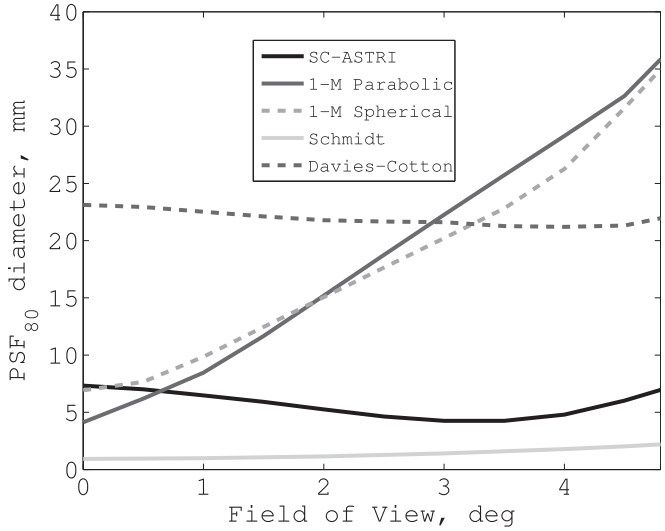

Figure 1. Linear size of the PSFs (diameter of the spot enclosing 80% of the PSF light) on the focal plane of the telescopes: single-mirror designs require the use of PMTs, while dual-element designs (Schmidt and SC) can exploit much more compact pixel solutions on the order of ∼3–6 mm.

control system. The SC solutions, entirely based on mirrors, remove the problem of the manufacturing and alignment of large refractive elements and also avoid the partial absorption of the UV portion of Cherenkov light spectrum by the frontal corrective plate. The drawbacks of an SC telescope are the more complex optics manufacturing, the presence of a large secondary mirror, and the position of the focal plane between M1 and M2. A picture of the ASTRI SST-2 M prototype is shown in Figure 2, and its main optical specifications are reported in Tables 2 and 3.

As shown in Tables 2 and 3, the ASTRI SST-2 M prototype has a slightly modified SC configuration since the M1–M2 separation is not exactly twice the effective focal length of the telescope as in the original solution proposed by Schwarzschild and Couder (Wilson 1994). The modified configuration, which introduces a contained astigmatism component, comes from a ray-tracing optimization process that takes into account the required plate scale, the corrected FoV, the segmentation of the focal plane, and the detector technology.

2.1. ASTRI Primary and Secondary Mirrors

Both the surfaces of M1 and M2 are even aspheres, and they are described by the classical polynomial equation used in optics:

$$z(r) = \frac{cr^2}{1+\sqrt{1-(1+k)c^2r^2}} + \sum_{i=2}^{N} \alpha_i r^{2i} \qquad (1)$$

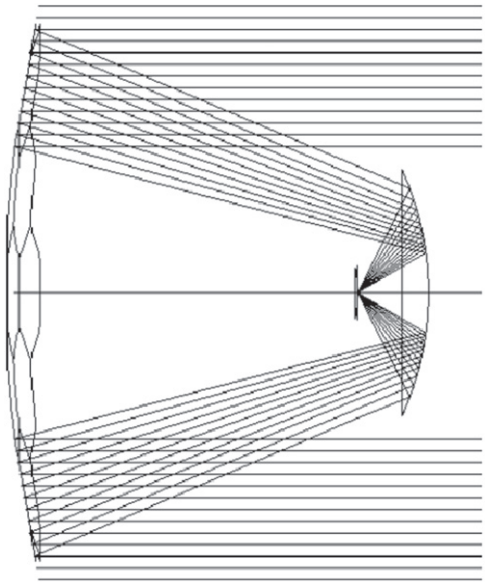

Figure 2. The ASTRI Schwarzschild–Couder configuration and the rays optical path for an on-axis source at infinity. The secondary mirror creates an important obscuration ratio and the focal plane of the telescope is curved and located between M1 (primary mirror) and M2 (secondary mirror).

Table 2
Geometry of the Three Main Optical System Components, M1, M2, and Camera in Terms of Diameter, Paraxial Radius of Curvature (RoC), Sag of the Surface Center-to-edge, and Relative Distances between the Elements

Surface	Aperture	RoC	Sag	Distance to
M1	4306 mm	−8223 mm	0–268 mm	M2: 3108 mm
M2	1800 mm	2180 mm	0–194 mm	DET: 520 mm
DET	360 mm	1060 mm	0–15 mm	…

Table 3
Main Telescope Optical Design Parameters

Telescope Parameters	Size
Effective focal length	2141 mm
Working $F/\#$	0.51
Field of View	9°6
Obscuration ratio[a]	∼40%
Plate scale	96″/mm
Angular magnification	−1.85

Note.
[a] Obscuration ratio (D_{M2}/D_{M1}).

with c as the paraxial curvature of the surface and k as the conic constant. The α_i terms are the aspherical coefficients that parameterize the sag deviations from a spherical profile.

The primary mirror surface is segmented in a mosaic of 18 hexagons subdivided into three different types, each having

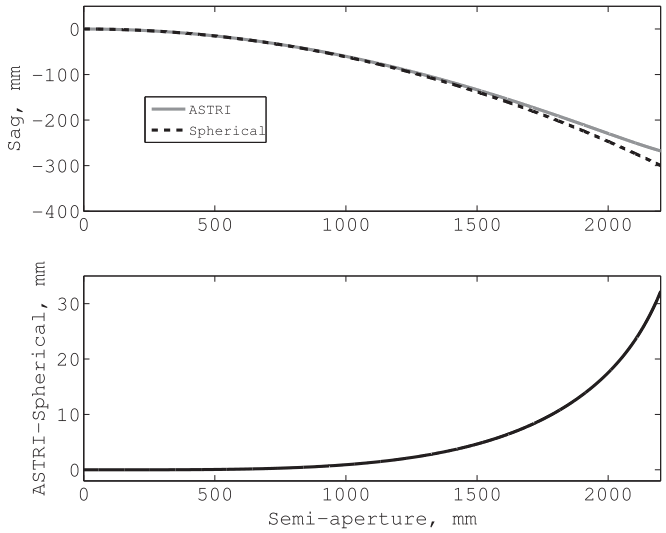

Figure 3. Top: M1 profile as a function of the radial aperture (solid gray line); the black dashed curve refers to the spherical surface with the same radial aperture and paraxial radius of curvature. Bottom: difference between the ASTRI M1 profile and a spherical mirror with the same paraxial radius of curvature.

different surface curvatures that change continuously from the paraxial to the marginal region and arranged into three different rings. This design comes from an optimization process targeted to preserve a constant PSF size along the FoV and is compatible with the SiPMs detectors, extremely small focal ratio, and the need for a reliable manufacturing process. This optimization process is based on a merit function developed using the commercial ray-tracing software Radiant Zemax. Each hexagon has an aperture of 849 mm edge-to-edge. The surface asphericity increases from the paraxial regions to the marginal ones as shown in Figure 3. M1 has a progressively flattened aspherical profile moving toward the outer rings: the nominal RoC of the inner ring is $R_{\text{paraxial}} \sim -8223$ mm while that of the outer is $R_{\text{marginal}} \sim -12738$ mm.

The secondary mirror is a monolithic surface with a diameter $D_2 = 1800$ mm and a paraxial RoC $R_2 = 2180$ mm. The aspherical profile of the mirror is described by Equation (1), and the amplitude of the aspherical coefficients is reported in Table 5. The sag profile of the surface is extremely steep: the maximum depth (center-to-edge) of the sag is ∼194 mm as shown in Figure 4.

3. The Hot Slumping Technique

For the manufacturing and replication of large and lightweight reflecting surfaces at a reasonable cost, the classical lapping techniques are not adequate. Moreover, IACT mirrors can tolerate surface root mean square (rms) errors $< 30\,\mu$m (Canestrari et al. 2013) that allow the use of alternative production technologies. In recent years, for the manufacturing

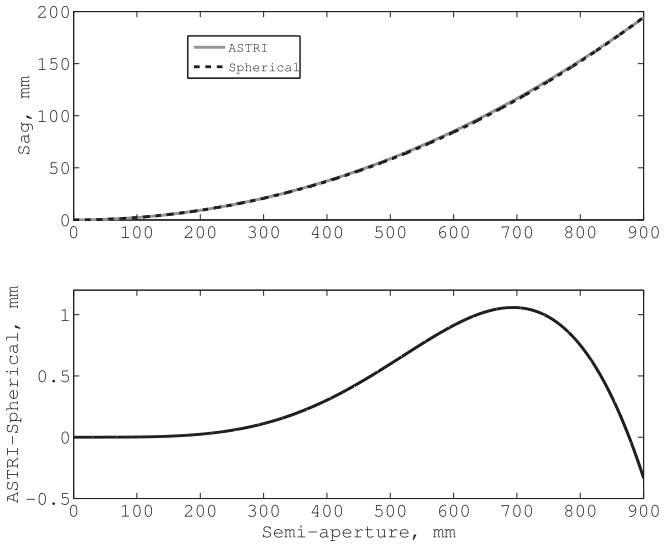

Figure 4. Top: radial profile of ASTRI M2 (solid gray line) and radial profile of the spherical mirror with the same paraxial radius of curvature (dashed gray). Bottom: residuals between ASTRI M2 and a spherical surface of equal diameter and paraxial radius of curvature. The asphericity of the sag increases in the middle-outer part of the mirror.

of IACT mirrors, techniques like diamond milling (Bastieri et al. 2005) and cold glass slumping (Pareschi et al. 2008) have been successfully implemented. While the production of M1 segments has been successfully carried out through the cold slumping approach, the manufacturing of the steep sag profile of M2 and the search for a monolithic design require the hot slumping technique. In general, with the hot slumping technique a thin and flat sheet of glass is positioned above a mold with the shape profile of the desired optical surface and by means of a thermal cycle in a oven, that changes the viscosity properties of the glass, it adheres and slumps onto the mold surface and assumes the shape of the mold. When the system is cooled down, the slumped glass is released from the mold and subsequently coated. A schematic representation of the process is shown in Figure 5.

Depending on the side of the mirror that is in contact with the mold, two approaches are distinguished: the direct approach, in which the optical surface of the mirror comes in contact with the mold during the process, or the indirect approach, in which the contact happens on the back side (Winter et al. 2010). The direct hot slumping requires that the mold has a very low surface micro-roughness to avoid changes to the glass. The process is executed in a clean room, since a dust grain trapped between the mold and glass surfaces during the slumping process prevents a correct copy of the shape of the mold in an area some cm^2 wide (Ghigo et al. 2009). To prevent errors to the shape of the glass, especially during the cooling phase, pressure is applied. A series of different thickness M2 prototypes have been produced for the ASTRI

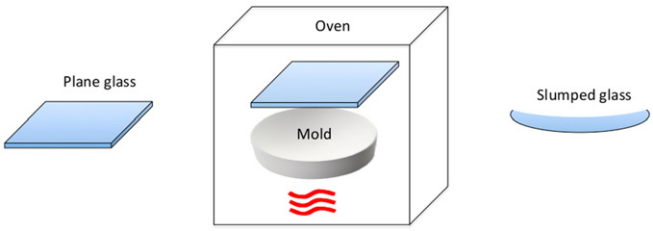

Figure 5. In the hot slumping process, a plane sheet of glass is heated up by a thermal cycle until it progressively adheres to the mold that imprints the desired optical profile. Once the room temperature is reestablished, the glass is released from the mold and it keeps the shape copied from the mold.
(A color version of this figure is available in the online journal.)

Table 4
Overall Budget of the Acceptable Tolerances in the Manufacturing Process of M2

Diameter	1800 mm ± 20 mm
Radius of curvature	2180 ± 6 mm
Focal length	1090 ± 3 mm
Sag	0 to 194 mm
Manufacturing	Value
Mold	120 μm PV[a]
Replication process	200 μm PV
Total	217 μm PV, quadratic propagation

Note.
[a] Peak to Valley.

Table 5
Aspherical Coefficients Amplitude That describe the Profile of M2 and Account for the Departure from the Spherical Profile Shown in Figure 4

Aspherical coefficients	Value
α_4	1.62076e-11
α_6	−2.89584e-17
α_8	8.63372e-24
α_{10}	3.34856e-30
α_{12}	−1.03361e-36
α_{14}	−6.73524e-43
α_{16}	−3.06547e-49
α_{18}	3.17161e-55
α_{20}	−3.71183e-62

SST-2 M prototype via indirect hot slumping that has the great advantage (with respect to a direct approach) of not requiring highly polished mold surfaces. The thickness of the mirror prototypes made of Borofloat glass are 19, 15, and 6 mm, and the manufactured prototypes of M2 have to be compliant with the tolerance requirements of the shapes given in Table 4.

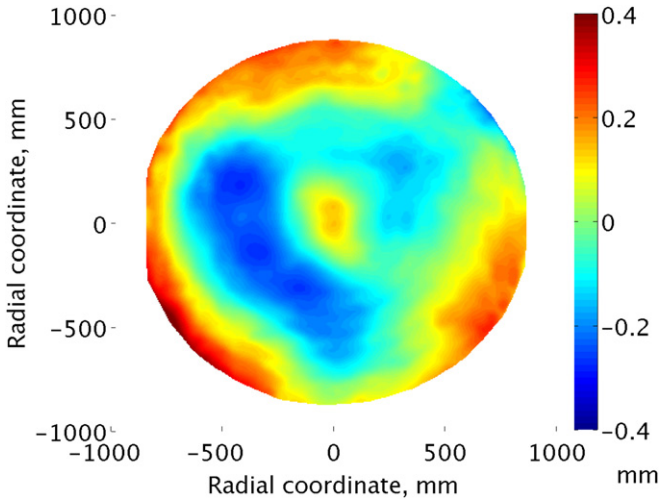

Figure 6. Residuals map of M2 prototype obtained with profilometry measurements, units are in mm. The map shows deviations from the nominal sag of PV ∼ 0.74 mm and surface rms ∼ 0.14 mm. The left–right and top–bottom edges of the map are incomplete.
(A color version of this figure is available in the online journal.)

A dedicated test campaign on the 19 mm prototypes (weight 130 kg) has been carried out as discussed in Section 4.

4. Secondary Mirror Qualification

This section is focused on the testing of the M2 prototype selected for the integration on the ASTRI SST-2 M prototype. Traditional qualification tests used for astronomical optics (e.g., interferometry) are unfeasible due to the large peak to valley (PV) typical of the Cherenkov optics. For this reason, two alternative tests, a profilometry analysis and a PSF measurement, have been recognized to assess the quality of the mirror prototypes. The main test results are discussed in Sections 4.1 and 4.2.

4.1. Profilometry Measurements

A first evaluation of the mirror quality has been carried out by a profilometry measurement. The machine used to measure the mirror profile is a Zeiss 3D coordinate measuring machine (model MZG 30 60 20, accuracy 7.5 μm along the z-axis). For each mirror prototype, a residuals map from the nominal sag of M2 has been obtained with the profilometer. The residuals map for the M2 prototype mounted on the ASTRI SST-2 M prototype is shown in Figure 6. 88.7% of the overall surface is inside the tolerances range (shape deviations $<$ 0.217 mm, PV), while 12.3% of the measured points shows deviations beyond the limit (PV ∼ 0.74 mm and rms ∼ 0.14 mm). The larger deviations (blue and red areas of Figure 6) are mainly concentrated in the outer parts and in some spotty intermediary regions. Due to the nature of the bending process, the outer parts of the glass are the most difficult to replicate from the mold and very often undergo deviations from the nominal sag. Due to a measuring machine limit, the map surface has a completeness $>$ 90%; as shown in Figure 6, the left–right and top–bottom edges of the mirror surface are missing.

A convenient representation of the 3D residuals map in the optical design model of the telescope is based on the Zernike polynomials (Noll 1976):

$$\Delta z(x, y, z) = \sum_{i=1}^{N} a_i Z_i(\rho, \phi) \quad (2)$$

with a_i as the amplitude coefficients and $Z_i(\rho, \phi)$ as the Zernike polynomials in polar coordinates. The measured residuals map of the M2 prototype (Figure 6) is interpolated and reproduced by a least squares fit with 231 Zernike terms (Figure 7). The polynomials series is truncated to the 231th Zernike term due to an internal limitation of the ray-tracing software used for the simulations that supports up to 231 terms. This upper limit prevents the representation of the highest spatial frequencies, but adequately describes most of the shape deviations of the mirror as proved by the accurate PSF simulations of Figure 14.

The interpolated residuals map obtained with 231 Zernike terms shows some deviations from the measured points especially in the outer regions of the mirror even if it has comparable $\mathrm{PV}_{\mathrm{Zernike}} \sim 0.73$ mm and surface $\mathrm{rms}_{\mathrm{Zernike}} \sim 0.12$ mm. The slightly lower rms is due to the smoothing of the residuals map by the use of a finite and limited number of Zernike terms. The percentage of the simulated surface out of specifications is around 10%. Although not all the mirror surface was measured, map completeness is ∼90%, not all the reflecting surface is active during the telescope observations; as shown in Figure 8, the light reflected from M1 does not cover the whole M2 surface, and the outer regions (more problematic for the slumping process) are only marginally illuminated.

Once the Zernike terms are calculated with a dedicated Matlab script, they are loaded in the optical design model of the telescope to check their impact on the overall system performances. This study is parameterized in terms of the telescope PSF size over the FoV. The aperture photometry of the PSFs is calculated by means of IDL routines, and the representative value for the evaluation is the so-called D_{80}, i.e., the diameter of the circle enclosing 80% of the PSF light. In Figure 9, the simulated PSFs over the FoV with the Zernike representation of M2 and for the nominal design are compared. In this simulation, M1 has its theoretical profile, but smaller sag errors are expected since the curvature radius of the surface is about five times larger with respect to M2 and the slumping process is more precise. Despite the general increase of the PSFs produced with the measured profile of M2, the telescope

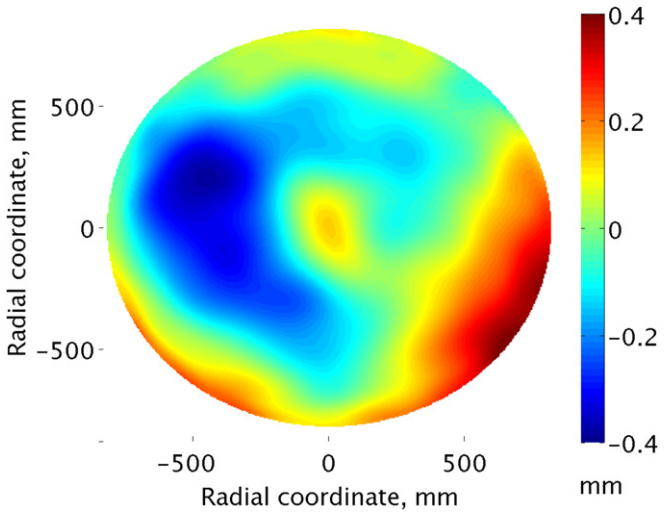

Figure 7. Residuals map of M2 prototype reconstructed on the basis of the profilometry data set by a series of 231 Zernike polynomials, units are in mm. The map is extrapolated to the entire physical radial aperture of the mirror. The Zernike map modifies some shape deviations of Figure 6 but preserves a good PV and rms compatibility ($PV_{Zernike} \sim 0.73$ mm and surface $rms_{Zernike} \sim 0.12$ mm).
(A color version of this figure is available in the online journal.)

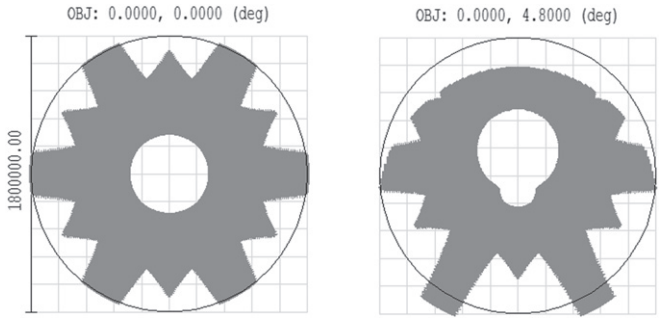

Figure 8. Light footprint onto the M2 surface for on-axis (left) and off-axis (right) source. The black circle around the light footprints is the M2 contour (diameter = 1.8e6 μm), and the central obscuration is due to the camera body. The light reflected from M1 does not completely illuminate M2, and the more problematic outer regions are marginally working.

is fully compliant with the requirement for SSTs that requires a telescope $PSF_{D80} < 0.^{\circ}25$ over 80% of the FoV.

4.2. M2 PSF Study

An independent test to assess the reliability of the Zernike representation of M2 and to characterize the mirror performances consists of the study of the mirror PSFs. This test is widely used in the qualification of IACT mirrors, and it allows the measurement of the PSF size and the estimate of the mirror focal length. Given the high asphericity of M2, more reliable information can be obtained by subdividing the mirror surface

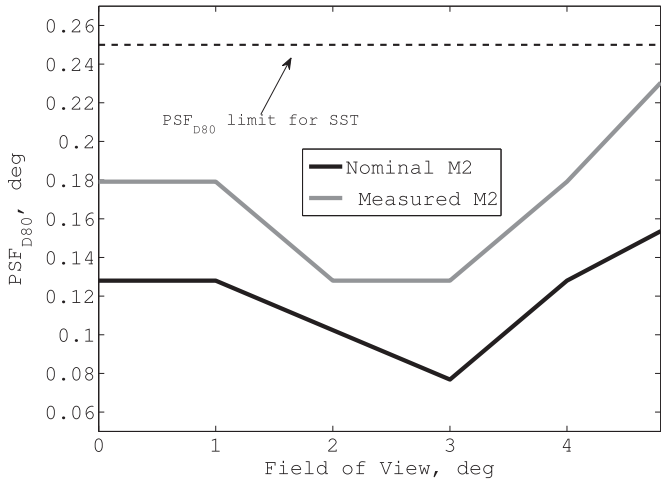

Figure 9. PSF_{D80} for the telescope with a nominal M2 design and for the measured M2 represented by 231 Zernike polynomials. The PSFs size profile is systematically above the nominal curve, but all the fields are below the limit fixed for SSTs. In this simulation, M1 has its theoretical sag profile.

into different subapertures. This is achieved by the use of cardboard spatial masks that obstruct all the optical surfaces but one ring of interest. With this technique, the measured PSF is averaged along a certain radial portion of the sag and along the overall azimuthal coordinate. A series of six spatial masks has been designed and fabricated for testing the M2 prototypes; the masks isolate sharp rings at different radii over the surface, as shown in Figure 10.

To perform the PSF measurements, the mirror is illuminated uniformly with an LED source positioned approximately at the mirror RoC (2f configuration); a CCD camera is used to image the PSF, and both the light source and the camera are kept specularly slightly off-axis (with respect to the mirror optical axis) to avoid vignetting of the former. Both the light source and the CCD camera are mounted on the same platform that can be moved to find the mirror best focus position (see Figure 11). The measurements scan the entire mirror focal region ($\sim 2f \pm \delta$) from an extra-focus position to an intra-focus configuration. The uncertainty of the platform positioning with respect to the mirror is $\sim$1 mm. The images are acquired by the CCD camera remotely controlled via USB interface and stored on a PC. Once the best focus position is identified, the focal length of the mirror is measured by the disto device.[5] Subsequently, the image frames are analyzed following the same procedure explained in Section 4.1 to extract the PSF photometry, R80 values, and best focus position. The goal of this test is twofold: measuring the PSFs and comparing them to the simulated spots and estimating the local RoC of each mirror ring.

[5] Device to measure the distance between two points from one location with a laser distance meter.

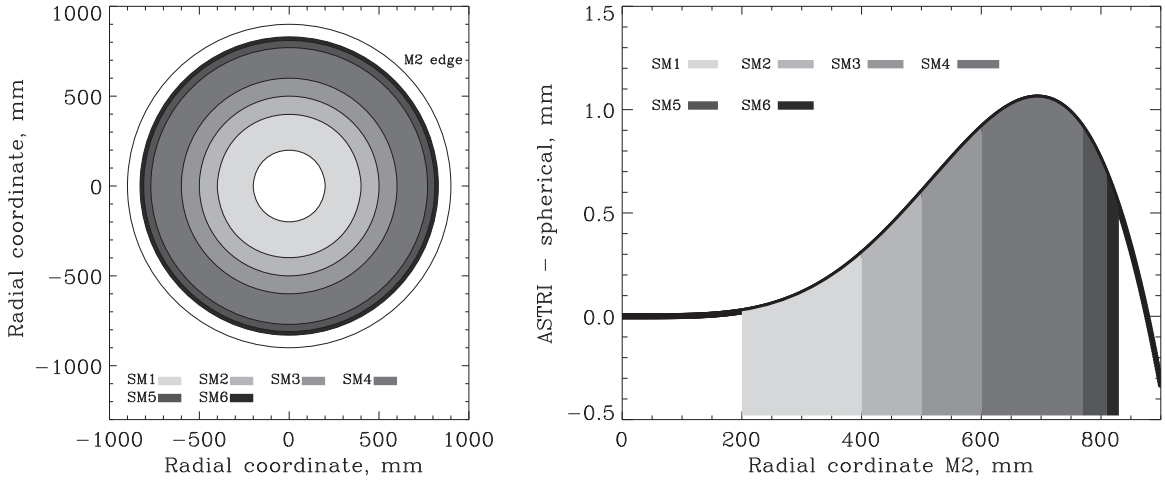

Figure 10. Left: schematics of the six cardboard spatial masks and their selective footprint on M2 surface. With reference to the plot on the right, the size of each ring is designed to illuminate a portion of surface over which the difference between the ASTRI M2 and a spherical mirror with the same paraxial RoC is $\Delta z < 0.3$ mm.

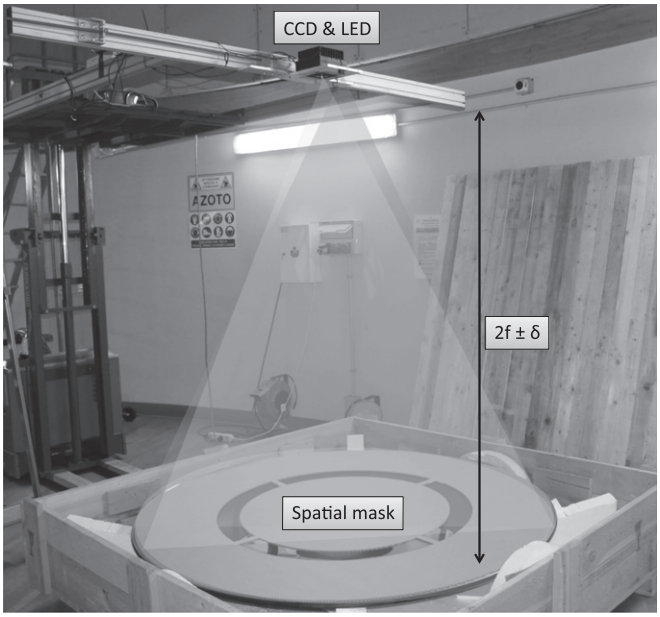

Figure 11. Picture of the setup operated during the M2 PSF study. The mirror is covered with a spatial mask; the CCD camera and the light source (LED) are suspended on a platform that can be triaxially moved with respect to the mirror being tested to explore different focal regions of the mirror ring.

The scan of the optical surface by the series of masks allows us to check the correspondence between the measured and the simulated PSFs, providing an excellent verification of the model built on the basis of the Zernike analysis and used for the simulations of the entire optical system. For each focal series with a certain spatial mask, a simulation with the same configuration, spatial mask, and the M2 Zernike representation is performed.

In the following, the results obtained from spatial mask 2 and 6 are presented in detail, for example, for the procedure followed with all the masks. Concerning mask 2, the PSF focal series are in excellent agreement with both the simulations (nominal and measured M2 sag) as shown in Figure 12. The focus depth of this ring is about 10 mm. Despite the little deviations that occur at some points, the ability of the simulations in reproducing even the smallest rims and ripples of the measured PSFs is remarkable (compare the PSFs in Figure 13). Mask 6 samples the outer aspherical regions of M2 that are the most critical parts to be copied from the mold. The focal series from mask 6 shows a discrepancy of 5 mm in the position of the best focus between the nominal and measured profiles (see Figure 12). The simulated focal series is in good agreement with the measured points as well as the simulated PSFs shown in Figure 14.

After best focus recognition for a certain ring, the focal length and the RoC are measured with the disto device. In Figure 15, the measurements of the RoC retrieved from the six spatial masks are plotted as a function of the average radial coordinate recognized by each spatial mask. The RoC for a given ring is averaged along the azimuthal coordinate and a certain radial interval, but for sufficiently sharp masks, it is well representative of the mirror ring being tested. Two spatial masks, masks 3 and 6, show deviations from the RoC of the nominal profile. The existence of deviations at mask 3 could be explained by the presence of a shape deviation (sag depression with respect to nominal design) at mid-radii shown in Figure 7, while deviations of mask 6 could be related to slumping imperfections at the edge of the mirror that are usually the most critical parts to copy from the mold. These two masks, however, account for only 16% of the overall M2 area.

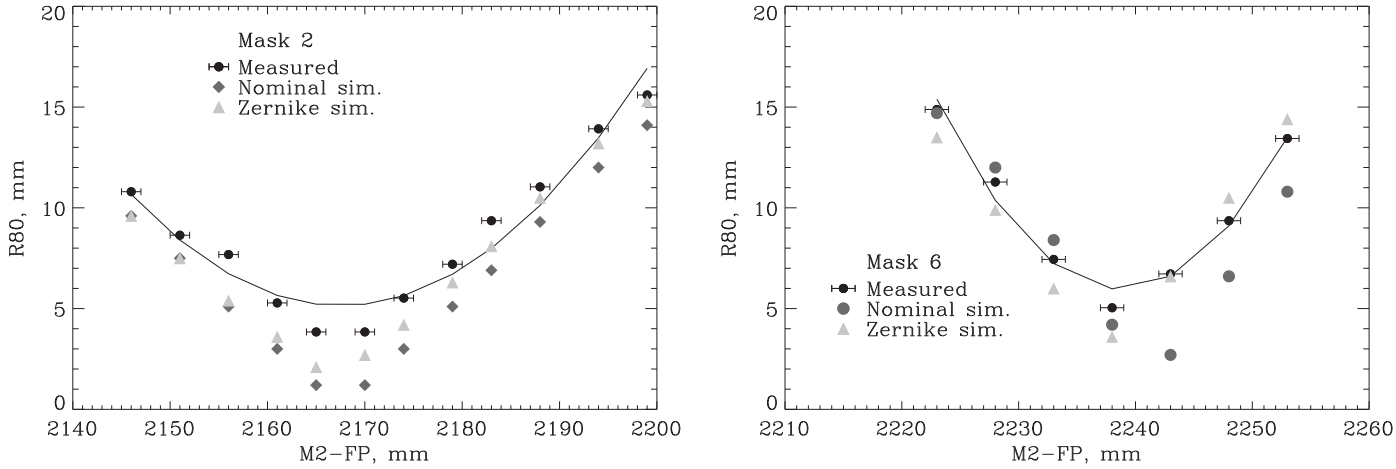

Figure 12. Left: PSF size (R80 = D80/2) for the focal series obtained with spatial mask 2; M2–FP is the separation between M2 and the focal plane. Measured points from extra-focus to intra-focus configuration (circles), simulated points for nominal M2 (diamonds), and simulated points for the Zernike representation of M2 (triangles). The curve interpolating the measured points is systematically above the theoretical simulated points, but the simulated points taking into account the residuals map precisely reproduce the trend of the measured points. The vertical error bars of the measured points are small and hidden by the circle marker. Right: focal series obtained with mask 6; there is a 5 mm discrepancy between measured and nominal best focus position of the focal series. Nevertheless, the simulated Zernike profile efficiently reproduces the deviations of the measured PSFs.

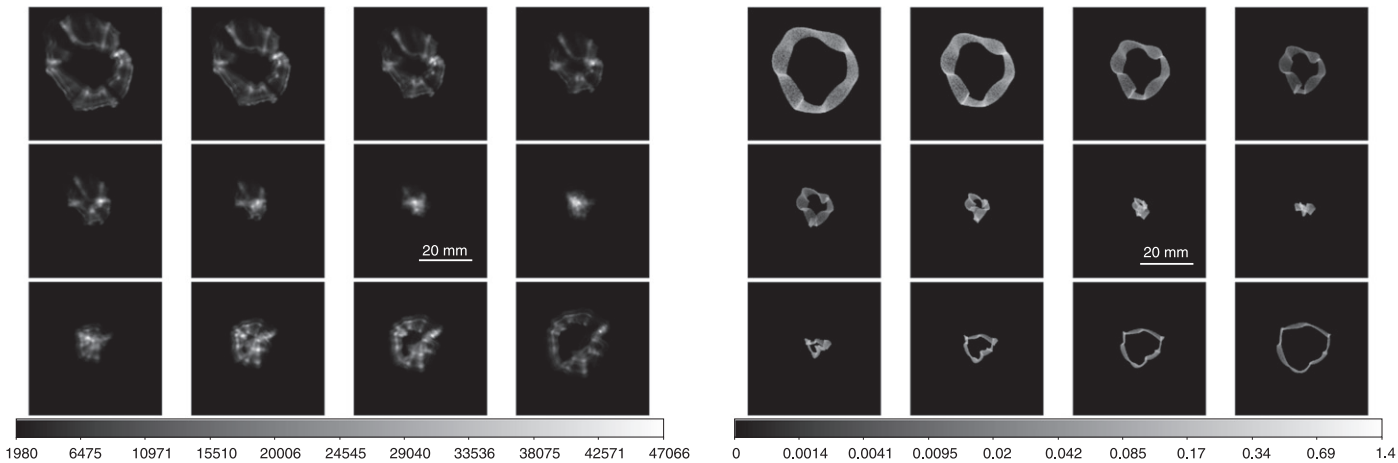

Figure 13. Left: focal series of the measured PSFs for spatial mask 2. From left top extra-focus to bottom right intra-focus PSFs, each extra-focus step, in both directions, is 5 mm. Right: focal series of the simulated PSFs by Zernike polynomials for spatial mask 2. From left top extra-focus to bottom right intra-focus PSFs, the simulated PSFs reproduce accurately the real PSFs shown on the left.

The PSF test efficiently validates the Zernike representation of M2 discussed in Section 4.1. All the measured focal series with different masks show a general broadening of the PSFs that, however, are closely reproduced by the M2 Zernike model and do not constitute a significant issue to the telescope performances as confirmed by the performance results in Figure 9.

5. Conclusions

The secondary mirror prototypes for the ASTRI SST-2 M are the result of a best-effort manufacturing process for the production of large, aspherical surfaces for astronomical applications. To our knowledge, these are the first mirror prototypes for astronomical applications realized with a hot slumping process at such large sizes. An extensive test campaign supported by accurate ray-tracing simulations has been carried out on the mirror prototype chosen for the integration to the ASTRI SST-2 M telescope. The model developed with the ray-tracing software is characterized by a slightly lower rms with respect to the measured data set that might lead to a more optimistic mirror representation. However, the model reproduces with good reliability both best

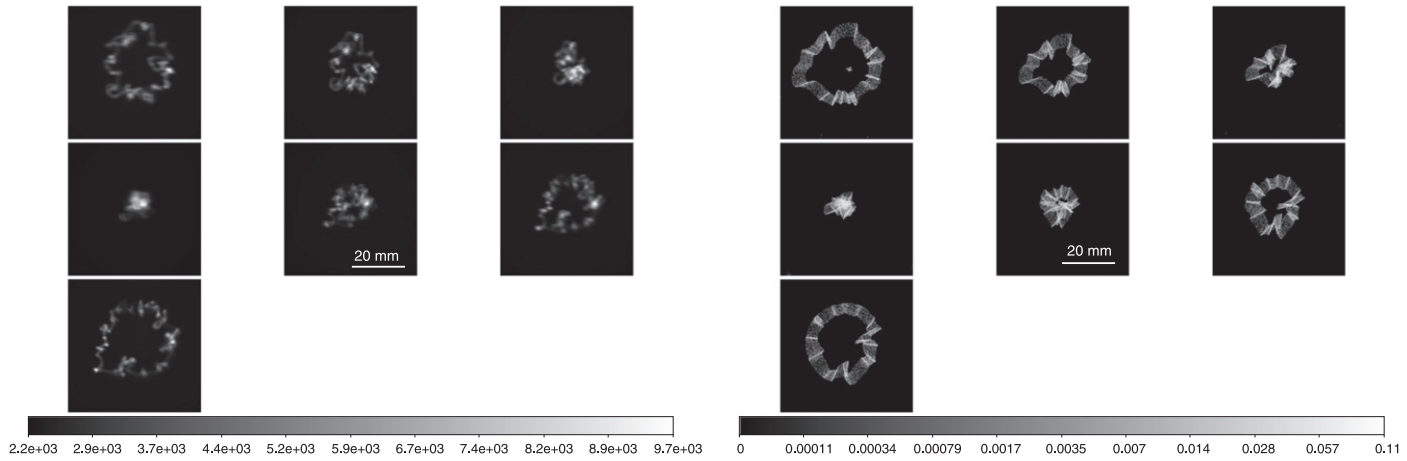

Figure 14. Left: focal series of the measured PSFs for spatial mask 6. From left top extra-focus to bottom right intra-focus PSFs (focus step 5 mm). Right: focal series of the simulated PSFs by Zernike polynomials. There are some discrepancies in the best focus position of the focal series that are visible both from the different PSFs topology and from the different minima position of the focal series in Figure 12.

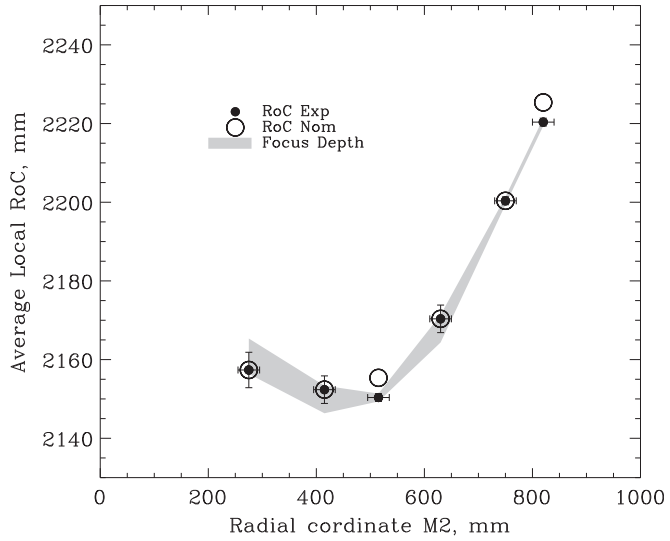

Figure 15. Average local radius of curvature for different spatial masks. The black dots are the estimated RoC from the measurements, the empty circles are the simulations with the nominal M2 sag profile, and the shaded gray area represents the measured focus depth of each ring. Two masks (3 and 6) show deviations from the nominal profile, but their weight in terms of area coverage is only 16% of the overall reflecting surface of the mirror.

and worst cases (e.g., mask 2 and mask 6). Both profilometry and PSF tests have led to a quantitative evaluation of the sag deviations from the nominal design. The level of nonconformity with respect to the nominal specifications is estimated in 12.3% of the overall surface, but there are interesting perspectives for improvement of the next large-scale production of mirrors related to the CTA Observatory. Moreover, even if not discussed in this paper, the shape deviations appear to be the same among all the manufactured mirror prototypes of different thickness (19, 15, and 6 mm), meaning that the reliability in replication process of the slumping technique is good. Slumping techniques also lead to a competitive cost with respect to the lapping and polishing procedures commonly used with the astronomical optics making them attractive in the perspective of a large array of telescopes. The effects of the shape deviations on the telescope performances have been assessed for different fields in the FoV, confirming the compliance of the telescope with the performance requirements issued by CTA already used for the current prototype mirror quality.

This work was partially supported by the ASTRI "Flagship Project" financed by the Italian Ministry of Education, University, and Research (MIUR) and led by the Italian National Institute of Astrophysics (INAF). We also acknowledge partial support by the MIUR Bando PRIN 2009 and TECHE 1.05.08. We are warmly grateful to A. Frigo, L. Traverso, G. Martorana, R. Vanni, V. Chiomento, M. Rebeschini, and Dr. L. Tomasella for the support to the testing operations at Asiago Observatory's Copernico Telescope. Authors are grateful to M. Riva, G. Tosti, M. C. Maccarone, J. E. Ward, J. Rico, and G. Maier for the precious suggestions and corrections to the manuscript. Authors are thankful to Gianni Quaia from EOT Company for the optical components donated in support of the qualification tests campaign. The corresponding author wishes to thank Prof. C. Barbieri and R. Mirzoyan for his continuous support on this work. The corresponding author is grateful to Dr. M. Pajola, I. Baronchelli, and L. Barilaro for the discussions on the IACT designs. Authors are deeply grateful to the anonymous referee who contributed to the improvement of the paper.

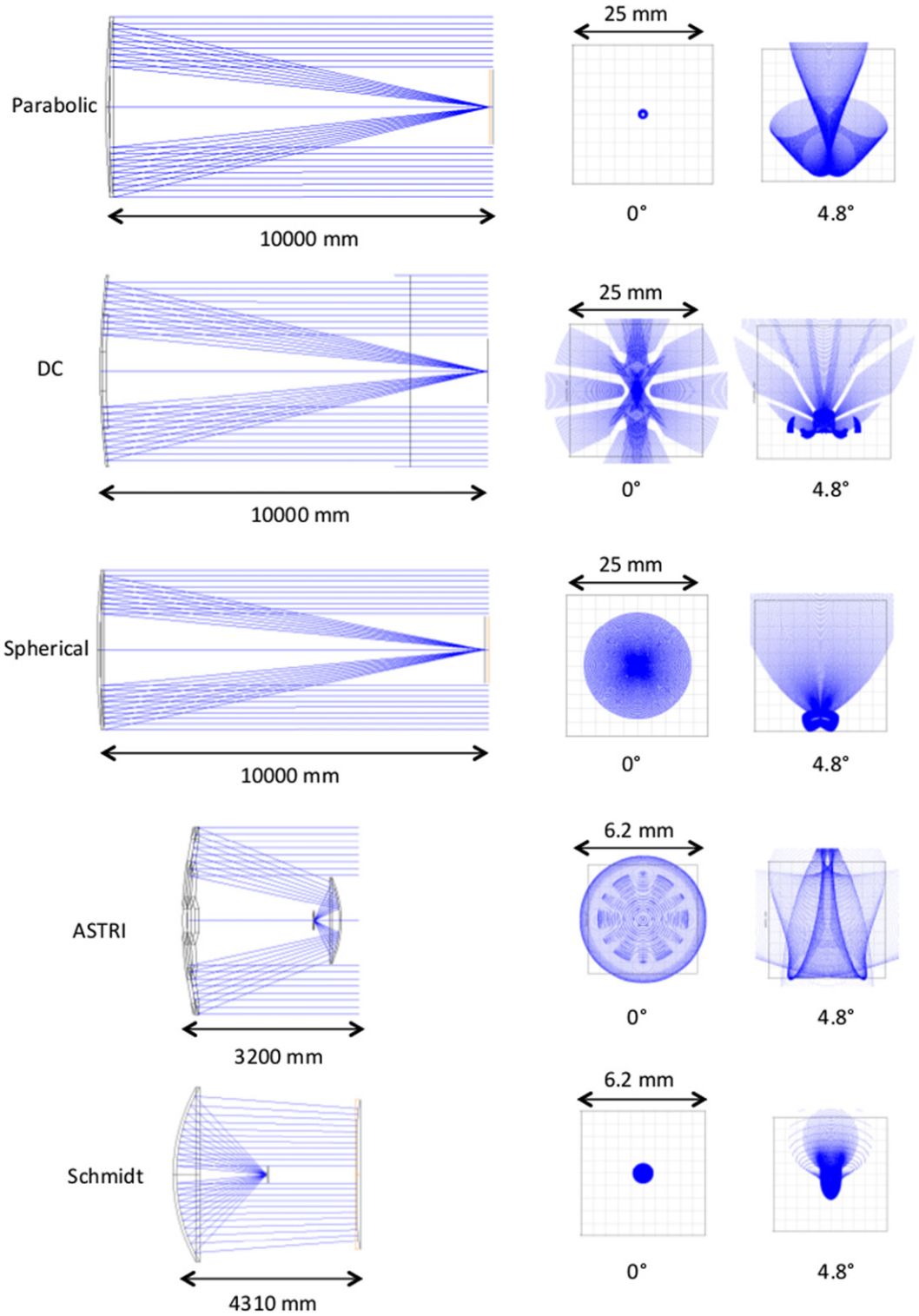

Figure 16. Schematics of the different 4 m class telescope optical configurations surveyed in the comparative study reported in Section 2. Left: optical design of the telescopes with the rays path inside the optics; the single-mirror solutions are less compact than the dual-element designs. Right: on-axis and off-axis (4°.8) PSFs compared to the typical size of the PMTs (25 mm) and of the SiPMs (3–6 mm).
(A color version of this figure is available in the online journal.)

Facilities: INAF Asiago Observatory's Copernico Telescope.

References

Acharya, B. S., Actis, M., Aghajani, T., et al. 2013, APh, 43, 3
Atwood, W. B., Abdo, A. A., Ackermann, M., et al. 2009, ApJ, 697, 1071
Bastieri, D., Agguiaro, D., Arnold, J., et al. 2005, Proc. ICRC (Pune), 00, 101
Bernlöhr, K., Carrol, O., Cornils, R., et al. 2003, APh, 20, 111
Biland, A., Bretz, T., Buβ, J., et al. 2014, JINST, 9, P10012
Canestrari, R., Cascone, E., Conconi, P., et al. 2013, Proc. SPIE, 8861, 886102
Davies, J. M., & Cotton, E. S. 1957, SoEn, 1, 16
De Angelis, A., Mansutti, O., & Persic, M. 2008, Nuovo Cim., 31, 4
Doro, M., Bastieri, D., Biland, A., et al. 2008, NIMPA, 595, 200
Ghigo, M., Basso, S., Canestrari, R., & Proserpio, L. 2009, Proc. SPIE, 7439, 74390M
Hillas, M. 1985, Proc. ICRC, 3, 445
Jelley, J. V., & Porter, N. A. 1963, QJRAS, 4, 275
Mirzoyan, R., & Andersen, M. I. 2009, APh, 31, 1
Noll, R. J. 1976, JOSA, 66, 207
Pareschi, G., Agnetta, G., Antonelli, L. A., et al. 2013, arXiv:1307.4962
Pareschi, G., Giro, E., Banham, R., et al. 2008, Proc. SPIE, 7018, 70180W
Tavani, M., Barbiellini, G., Argan, A., et al. 2008, NIMPA, 588, 52
Vassiliev, V. V., Fegan, S., Brousseau, P., et al. 2007, APh, 28, 10
Weekes, T. C., Badran, H., Biller, S. D., et al. 2002, APh, 17, 221
Wilson, R. N. 1994, RvMA, 7, 1
Winter, A., Vongehr, M., & Friedrich, P. 2010, Proc. SPIE, 7732, 77320B